

Video Article

Atom Probe Tomography Studies on the Cu(In,Ga)Se₂ Grain Boundaries

Oana Cojocaru-Mirédin¹, Torsten Schwarz¹, Pyuck-Pa Choi¹, Michael Herbig¹, Roland Wuerz², Dierk Raabe¹¹Department of Microstructure Physics and Alloy Design, Max-Planck-Institut für Eisenforschung GmbH²Zentrum für Sonnenenergie- und Wasserstoff-Forschung Baden-Württemberg (ZSW)Correspondence to: Oana Cojocaru-Mirédin at o.cojocaru-miredin@mpie.deURL: <http://www.jove.com/video/50376>DOI: [doi:10.3791/50376](https://doi.org/10.3791/50376)

Keywords: Physics, Issue 74, Chemistry, field theory (physics), crystallography, semiconductor materials, solid state physics, condensed matter physics, thin films (theory, deposition and growth), crystal defects, crystal structure (semiconductors), Thin-film solar cells, Cu(In,Ga)Se₂, grain boundary segregation, pulsed laser atom probe tomography, transmission electron microscopy, TEM, electron backscatter diffraction, atom probe tomography, APT, SEM, imaging

Date Published: 4/22/2013

Citation: Cojocaru-Mirédin, O., Schwarz, T., Choi, P.P., Herbig, M., Wuerz, R., Raabe, D. Atom Probe Tomography Studies on the Cu(In,Ga)Se₂ Grain Boundaries. *J. Vis. Exp.* (74), e50376, doi:10.3791/50376 (2013).

Abstract

Compared with the existent techniques, atom probe tomography is a unique technique able to chemically characterize the internal interfaces at the nanoscale and in three dimensions. Indeed, APT possesses high sensitivity (in the order of ppm) and high spatial resolution (sub nm).

Considerable efforts were done here to prepare an APT tip which contains the desired grain boundary with a known structure. Indeed, site-specific sample preparation using combined focused-ion-beam, electron backscatter diffraction, and transmission electron microscopy is presented in this work. This method allows selected grain boundaries with a known structure and location in Cu(In,Ga)Se₂ thin-films to be studied by atom probe tomography.

Finally, we discuss the advantages and drawbacks of using the atom probe tomography technique to study the grain boundaries in Cu(In,Ga)Se₂ thin-film solar cells.

Video Link

The video component of this article can be found at <http://www.jove.com/video/50376/>

Introduction

Thin-film solar cells based on the chalcopyrite-structured compound semiconductor Cu(In,Ga)Se₂ (CIGS) as the absorber material have been under development for more than two decades because of their high efficiency, radiation hardness, long-term stable performance, and low production costs¹⁻³. These solar cells can be fabricated with only little material consumption due to the favorable optical properties of the CIGS absorber layer, namely, a direct bandgap and a high absorption coefficient^{1,2}. Absorber films of only a few micrometers in thickness are sufficient to generate a high photocurrent. Since the diffusion paths of photogenerated charge carriers to the electrodes are relatively short, CIGS absorbers can be produced in polycrystalline form. The maximum efficiency of a Cu(In,Ga)Se₂ (CIGS) solar cell achieved so far is 20.4%⁴, which is the highest value among all thin-film solar cells.

To further establish the CIGS thin-film photovoltaic technology, both the reduction of production costs and the enhancement of solar cell efficiency are essential. The latter is strongly dependent on the microstructure and chemical composition of the CIGS absorber layer. Internal interfaces, in particular grain boundaries (GBs) within the absorber, play a pivotal role, as they can affect the transport of photogenerated charge carriers.

One of the main unresolved issues with respect to CIGS solar cells is the benign nature of CIGS GBs, *i.e.* polycrystalline CIGS absorber films yield outstanding cell efficiencies despite a high density of GBs and lattice defects.

Several authors studied GBs in solar-grade CIGS films with respect to their electrical properties^{5,6}, character and misorientation⁷⁻⁹ as well as impurity segregation¹⁰⁻¹³. However, no clear link between these properties could be established so far. In particular, there is a substantial lack of information regarding the local chemical composition and impurity content of the GBs.

In the past two decades, Atom Probe Tomography (APT) has emerged as one of the promising nano-analytical techniques¹⁴⁻¹⁷. Until recently APT studies of solar cells have been largely restricted by difficulties in the sample preparation process and the limited capability of analyzing semiconductor materials using conventional pulsed-voltage atom probes. These restrictions have been largely overcome by the development of the 'lift-out method' based on focused ion beam (FIB) milling¹⁸ and the introduction of pulsed laser APT¹⁶. Several papers about APT characterization of CIGS solar cells have been published¹⁹⁻²³, which are strongly encouraging for further investigations.

This paper gives a guideline of how to study internal interfaces in CIGS thin-film solar cells by the atom probe tomography technique.

Protocol

1. CIGS Layer Deposition

1. Sputter-deposit 500 nm of molybdenum (back contact layer) onto a 3 mm thick soda lime glass substrate (SLG).
2. Co-evaporate 2 μm of CIGS in an inline multistage CIGS process²⁴. The obtained CIGS layer deposited on Mo back contact is shown in **Figure 1**.
3. Measure the integral composition of CIGS layer by X-ray fluorescence spectrometry (XRF). The obtained CIGS composition is shown in **Table 1**.

2. Site-specific Samples Fabrication for APT Analysis

1. Cut a TEM Mo grid into two halves in order to obtain a row of several pins, being the support for the later specimens. Mount the TEM half-grid onto a holder and taper the ends of the pins by electropolishing in 5 wt. % NaOH down to a tip diameter $<2\ \mu\text{m}$. The process can be reasonable controlled using a stereoscope. Then mount the electropolished grid onto another holder that is optimized for sequential FIB, TEM, EBSD, and APT characterization.
2. Mill two trenches into the CIGS thin-film using FIB to get an undercut (**Figure 2a**). Make a first free-cut on the left side of the chunk.
3. Attach the micromanipulator to the chunk by depositing a Pt weld by ion-beam induced chemical vapor deposition. Then, make the final free-cut on the opposite site and lift-out the free-standing chunk (**Figure 2b**).
4. Cut now the sharp pins of the TEM Mo half-grid to a wedge (2-3 μm in diameter) having a good joint for the extracted chunk. Mount the chunk on the pins using Pt deposition (**Figure 2c**). Make a free-cut to finally obtain only a small part of the chunk (around 2 μm) on the top of the Mo pin. Afterwards mount the grid holder upside down and fill the gap between the Mo pin and the mounted piece with Pt. Pursue the same procedure with the remaining chunk. For more details about the lift-out procedure, the reader may consult the following references^{18,25}.
5. Place the grid upright and clean the cross-section of the chunk (choose the site with thinner Pt weld) by using a low accelerating voltage and beam current (5 kV and $<50\ \text{pA}$) in the FIB. Thus one gets a smooth surface and less contamination due to Ga^+ implantation, which is required for EBSD measurements.
6. From the EBSD measurement performed on the cross-section choose a GB of interest. The orientation of the GB is preferable to be perpendicular with respect to the analysis direction in the atom probe (z-axis) to reduce the local magnification effect²⁶, which is described more in detail in discussion part. An appropriate area with a GB is highlighted in **Figure 2d**.
7. Perform an annular milling in the area of the GB selected in step 2.6) to form a sharp tip. The radius of curvature should be small enough ($<100\ \text{nm}$) for further TEM investigations. To reach this goal, reduce the inner diameter of the annular milling pattern step by step (**Figure 2e**) and concomitantly visualize the tip shaping by secondary electron (SE). Thus one can correct beam shifts or adjust the milling pattern to remove irregularities on the tip like ripple or redeposition of material originating from different sputter yields, shadowing effects *etc.*
8. Localize the precise position of the GBs with respect to the apex of the tip by using the TEM tool (see **Figure 2f**), knowing that compared with other materials (like superalloys) the CIGS GBs are not visible in SEM.
9. Knowing precisely where the GB is located within the APT tip, transfer the specimen back to the FIB and continue to mill the sample to situate the GB at maximum 200 nm below the apex of the tip. At this stage, the milling is done at very low kV (5 kV) and low current ($<50\ \text{pA}$). Indeed, the goal is not only to localize the GB closer to the apex of the tip, but also to minimize the Ga^+ damage of the APT tip during this procedure. Concomitantly to the low-kV milling, visualize the shape of the APT tip in SEM and control the amount of the material which should be removed from the apex of the tip (**Figure 2g**).
10. Transfer again the specimen to the TEM and check the position of the GB with respect to the apex of the tip. Make an overview image of the specimen (**Figure 2h**) to obtain precise knowledge about the GB position, the evolution of the specimen diameter and the half shank-angle. This is necessary to achieve an optimal reconstruction of the APT data. Furthermore, use low magnifications and reduced exposure times to minimize electron-beam induced damages and C contamination which can lead to a higher failure rate in the APT measurements.

3. APT Analysis in a CAMECA LEAP 3000X HR System

1. Mount the specimen in the APT holder. Then, mount the specimen puck in one of the four carousels available.
2. Insert the carousel containing the specimen puck inside the load lock and start pumping the load lock. When the vacuum inside the load lock is $\sim 10^{-7}$ Torr, insert the carousel inside the buffer chamber.
3. After waiting ca. 1 hr to restore the vacuum in the buffer chamber ($\sim 7 \times 10^{-9}$ Torr), transfer the specimen from the buffer chamber to the main analysis chamber. This is done with a horizontal transfer rod, which is a manually operated device.
4. Before starting the measurement inside the APT, cool down the temperature to 60 K. This low temperature will avoid the diffusion of the atoms at the surface of the specimen during the analysis. We note here that 60 K is the set temperature and not the real temperature measured on the APT tip, which should be higher due to the laser heat of the specimen. As proposed by Kellogg *et al.*²⁷, this temperature can be estimated by taking into account the relative charge-state-ratio. Unfortunately, in this work the real temperature of the tips couldn't be calculated mainly because the field evaporation of the CIGS material is unknown.
5. APT experiments are carried out in laser mode using a green laser with a wavelength of about 532 nm and 12 psec pulse length.

4. Reconstruction of APT Data

1. Open the RHIT file (raw data directly obtained after APT measurements) with CAMECA's Integrated Visualization and Analysis Software (IVAS 3.6.2)²⁸ generally used to reconstruct the 3D map.
2. Perform the reconstruction of the 3D map using the following eight steps²⁸:

1. Step 1- *setup* which is a read-only pane giving all the details about the nature and the content of the selected study.
2. Step 2- *select ion sequence range*. This step defines the ion-sequence range relative to specimen-voltage to be selected in the reconstructing data.
3. Step 3- *select detector ROI*. This step gives the opportunity to remove the ions located outside the detector ROI (black ellipse on the detector event histogram).
4. Step 4- *TOF corrections*. This step computes the voltage, the time-of-flight (TOF), and the planarity of the detector ('bowl correction') corrections for the analysis.
5. Step 5- *Mass calibration*. The measured peak position in the analyzed mass spectrum is calibrated with known isotope/charge states.
6. Step 6- *Ranged ion assignment*. In this step the peaks in the mass spectrum are assigned to element isotope ranges.
7. Step 7- *Reconstruction*. This step applies one of three reconstruction methods to the data acquired: voltage method, shank-angle method or tip-profile method. The last one is used in current study to reconstruct our 3D-map. This method requires an SEM or TEM image of the tip, as shown in **Figure 2g** and **Figure 2h**. The tip radius at any point in the reconstruction is defined by a linear interpolation between a series of points defined in the SEM image.
8. Step 8- *Confirmation*. In this step, the preview created in the reconstruction tab is converted to a saved analysis.

Representative Results

Figure 3 shows a side view (x-z slice) elemental map of the random high-angle GB (HAGB) $28.5^\circ\text{-}\langle 511 \rangle_{\text{cub}}$ selected in **Figure 2** by site-specific preparation method. Co-segregation of Na, K, and O at a CIGS HAGB is directly mapped using APT. These impurities most likely diffused out of the SLG substrate into the absorber layer during the deposition of the CIGS layer at $\sim 600^\circ\text{C}$.

Figure 4a shows the Cu, In, Ga, and Se concentration profiles across the GB shown in **Figure 3**. The Cu, In, Ga, and Se concentrations at the GB are different to those in the grains interior (GIs). It can clearly be seen that Cu and Ga are depleted at this GB, whereas In is enriched. This is in agreement to what was postulated by Persson *et al.*²⁹ on the basis of *ab-initio* density functional theory (DFT) calculations, namely that Cu vacancy rows are preferentially formed at the CIGS GBs. The In enrichment and the Cu depletion could be explained by the low formation energy of the charge neutral defect pair $2V_{\text{Cu}} + \text{In}_{\text{Cu}}^{2+}$ ³⁰. It should be noted that the DFT calculations by Persson *et al.*²⁹ were done for a symmetrical GB (Σ_3 (112) TB), whereas the APT data in **Figure 3** was obtained for a random HAGB. Furthermore, Cu-enriched and In-depleted HAGBs were also observed for the same material as mentioned in our previous work²¹.

Figure 4b shows the concentrations of Na, K, and O impurities at this HAGB, which are 1.7 at %, 0.035 at %, and 0.4 at %, respectively (see **Table 2**). The corresponding interfacial excesses (Γ) values for Na (Γ_{Na}), K (Γ_{K}), and O (Γ_{O}) calculated from APT data are also shown in **Table 2**. These interfacial excesses were calculated using Cahn approach³¹.

The average compositions of GI₁ and GI₂ (GI: grain interior, see **Table 2**) show a slight variation of Cu, In, Se, and Ga concentrations from one grain to another. These concentration values are in good agreement with the concentration profiles in **Figure 4a**. Furthermore, the O concentration is different from one grain to another (170 ppm for GI₁ and 0 ppm for GI₂) whereas, the Na composition is almost constant (50 ppm for GI₁ and 60 ppm for GI₂, see **Table 1**). The K concentration inside the grains is below the noise level of this APT measurement (noise level = 45 ± 5 ppm/a.m.u.) and thus below the detection limit.

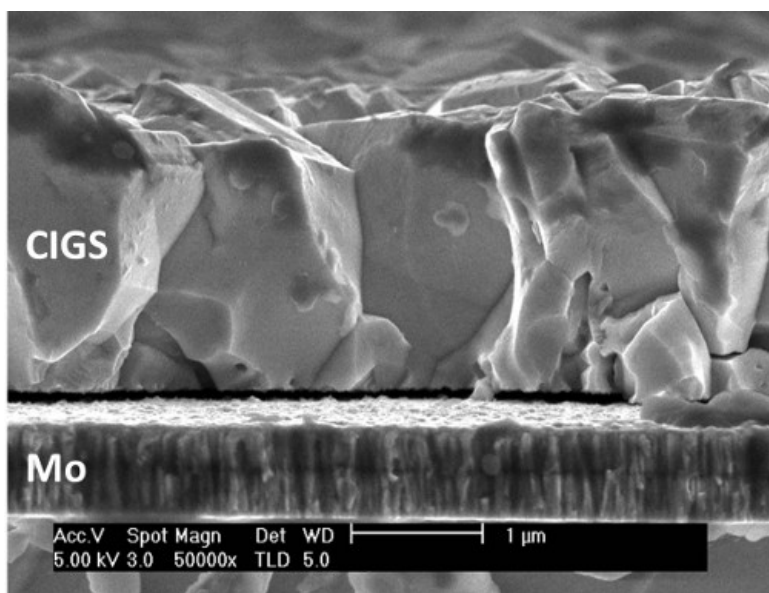


Figure 1. SEM image of a CIGS layer on Mo coated soda lime glass substrate.

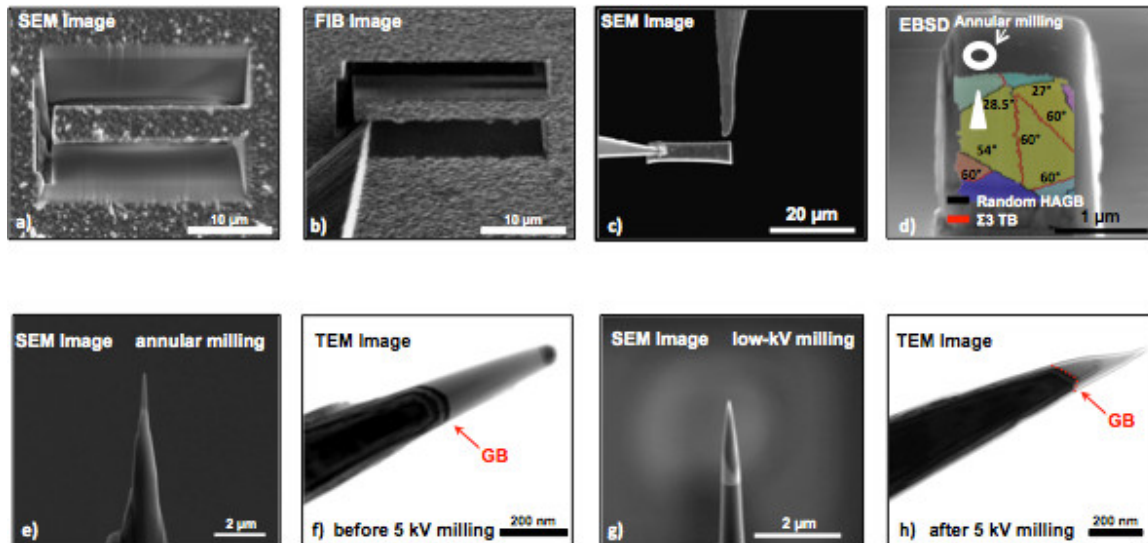


Figure 2. a) Milling of a chunk for lift-out, b) attaching of a micromanipulator by Pt deposition, c) mounting of a chunk piece on a TEM Mo half-grid, d) EBSD measurement on a cleaned cross-section, e) annular milling of a pre-sharpened tip, f) TEM image of a GB g) final low-kV milling, h) TEM image of a GB in the APT tip after low-kV milling. [Click here to view larger figure.](#)

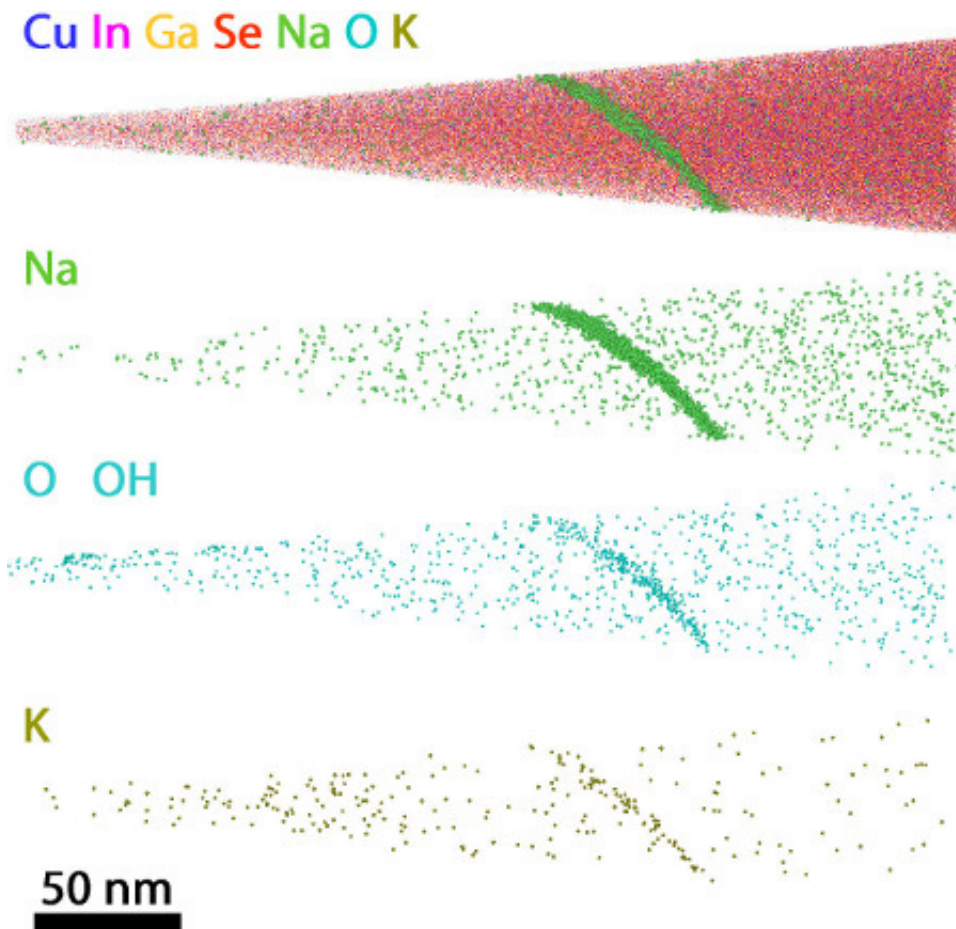


Figure 3. 3D APT maps of Cu (blue), In (pink), Ga (yellow), Se (red), Na (green), O and OH (light blue), and K (khaki). These 3D maps directly show Na, K and O segregation at a HAGB (28° - $\langle 511 \rangle_{\text{cub}}$), which was analyzed by EBSD and TEM prior to the APT analysis.

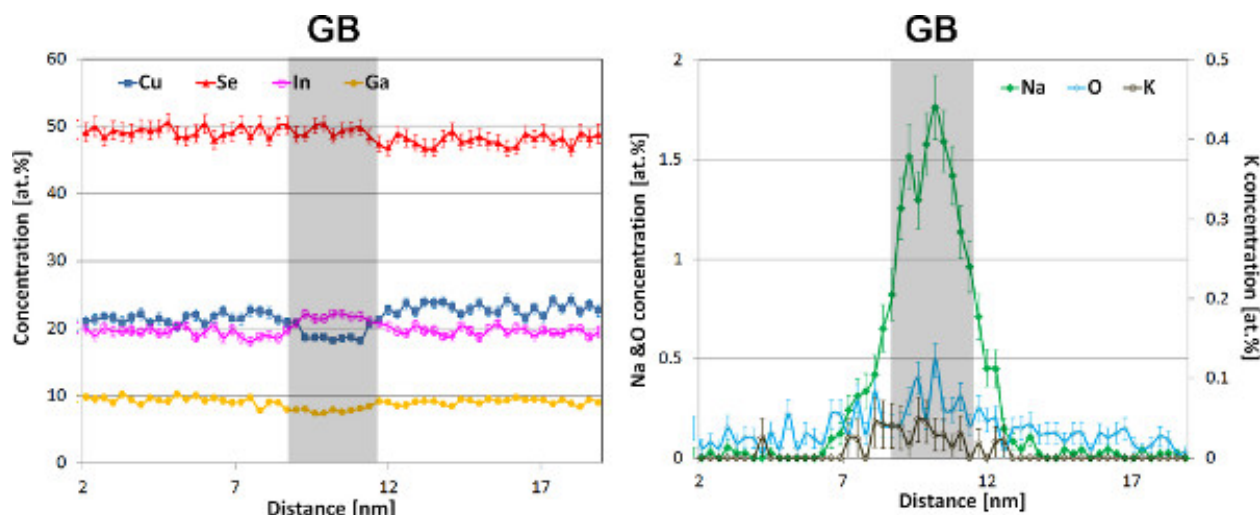


Figure 4. (a) Cu, Se, Ga, In and (b) Na, K, O concentration depth profiles through the GB shown in Figure 3. The sampling box used to build these profiles is 32 x 32 x 0.3 nm³. Bars give the statistical errors (2σ). [Click here to view larger figure.](#)

Element	Cu	In	Ga	Se
Conc. (at %)	22.3	18.6	7.2	51.9

Table 1. Integral composition of CIGS layer measured by XRF.

Elements	GI ₁ (at.%)	GI ₂ (at.%)	GB (at.%)	Γ _{GB} (at/m ²)
Cu	21.5±0.12	22.8±0.12	18.2 ±0.4	-
In	19.6±0.12	19.4±0.12	21.8±0.4	-
Ga	9.0±0.09	9.6±0.09	8±0.3	-
Se	49.7±0.1	48.1±0.15	49±0.5	-
Na	0.005±0.002	0.006±0.002	1.7±0.1	2.9 x 10 ¹⁸
K	-	-	0.035±0.01	7.5 x 10 ¹⁶
O	0.017±0.004	-	0.4±0.07	8.4 x 10 ¹⁷

Table 2. Cu, In, Ga, Se, Na, K, and O composition values in the grain interior (GI) and at the grain boundary (GB) of CIGS obtained from APT mass-to-charge spectra, after deconvolution of overlapping mass peaks. Γ_{GB} represents the interfacial excesses (Γ) at the GB.

Discussion

In the current work, we have presented APT results on a random HAGB in CIGS, a compound semiconductor material used for photovoltaic application. Furthermore, we have also shown that APT in conjunction with complementary techniques, such as EBSD and TEM, is a powerful tool to elucidate the structure-composition properties relationship for the CIGS solar cells. Unfortunately, the correlation between APT and EDX/EELS in TEM was not possible because firstly, EDX/EELS has not sufficient resolution to detect low Na and O concentrations at the grain boundary and secondly, EDX/EELS is not sensitive to all elements, especially for Na and O.

APT is a unique technique able to chemically characterize the interfaces at the nanoscale and to visualize them in three dimensions¹⁴⁻¹⁷. Highly dilute impurity concentrations in the tens of ppm can be detected because of the high signal-to-noise ratio in the mass spectra. Another advantage of APT technique is that the detection sensitivity is not element-specific if appropriate measurement parameters are selected.

One needs to mention here that to measure accurately compositional values at CIGS GBs and in grain interiors, it is important to choose the optimum conditions for APT analysis (temperature, laser energy, pulse rate, etc). If not, artifacts such as preferential evaporation and retention³² of elements may occur during the pulsed field evaporation of the specimen. These artifacts may show up when there is a large difference in field evaporation of the elements. Thus, the field evaporation rate, the voltage, and the laser energy should be set in such a way that all elements will be removed with equal probability. As shown here, by choosing correspondingly appropriate parameters for APT analysis, we found close CIGS composition compared to the one obtained by XRF (see **Tables 1 and 2**). We note here that the overestimation of the Se concentration in CIGS by XRF is due to the MoSe₂ layer present at the CIGS/Mo interface. A second reason for the lower Se concentration measured by APT (below the nominal value of 50%) might be the preferred evaporation of Se between the laser pulses as Se is the most volatile species in CIGS. Furthermore, the difference in Cu, In, and Ga concentrations between APT and XRF is due to the fact that APT measures the CIGS composition locally, whereas XRF measures an averaged composition of the CIGS film. Indeed, it is well known that the Cu/In concentration varies from one grain to another and the Ga concentration is higher in the upper part of the film (where our APT tip was prepared) due to the Ga gradient

observed in the multistage grown film³³. We note here that no Ga ions coming from the FIB source were observed in the mass spectrum (Ga from the FIB is found only as isotope 69 amu) and this is due mainly to the low-kV milling of the APT tips.

One main drawback which is observed when studying the interfaces with APT technique is that in general the width of the GBs, are either enlarged or reduced compared with the structural width calculated from TEM images (lower than 1 nm). This is due to the local magnification effect²⁶. This effect occurs when the GB has an evaporation field different from the bulk material. A GB with a higher evaporation field (E) leads to a protuberance at the tip surface ($E \sim V/R$, V is the applied voltage and R the radius of curvature). In this case the ions originating from the GB deflect outwards, which causes an apparent decrease in density of ions. Conversely, when the GB has a lower evaporation field the surface of the tip in the region of the GB will be flattened which deflect the ion trajectories inwards. In this case, the local density in the GB region will be higher. In addition, the trajectories overlap caused by the local magnification effects will also deteriorate the lateral spatial resolution at the interface, though the concentrations remain almost unchanged as shown by De Geuser *et al.*³⁴.

In the current study, the width of the detected random HAGB segregation zone (≈ 3 nm) is larger than 1 nm, the typical structural width of a GB. Furthermore, the atomic-density measured by APT is higher at the GB than in the CIGS matrix which indicates that the local magnification effect had occurred during the evaporation. The higher density at the GB is explained by the lower field evaporation of this particular CIGS GB compared with CIGS grains. For single charged ions, the field evaporation values are $F_{Cu} = 30$ V/nm, $F_{In} = 12$ V/nm, $F_{Ga} = 15$ V/nm, and $F_K = 60$ V/nm³⁵. The Se, Na, and O field evaporation values are not given in the literature. We note here that these values are valid for pure elements. In compound semiconductors, such as CIGS, the evaporation of each of these elements may be different. Nevertheless, in **Figure 4a** we found that the GB contains a lower Cu concentration than present in the grain interiors. Indeed, this lower Cu concentration may decrease the evaporation field at the GB. Furthermore, Letellier *et al.*³⁶ reported for nickel-based superalloys that the local magnification effect increases continuously as the GB approaches an orientation parallel to the tip axis (z axis). This may explain why the width of the GB is only slightly enlarged compared to other studies³⁷.

In conclusion, APT studies provide not only a 3D redistribution map of the elements, but also the chemical composition of the interfaces at the nanoscale. As many tools performing studies at the nanoscale, a particular attention should be paid to the analysis quality and data interpretation. Indeed, APT possesses some limitations as well and therefore it is important to understand how these limitations influence the measured data to ensure a correct data interpretation.

Disclosures

The authors have nothing to disclose.

Acknowledgements

This work is funded by the German Research Foundation (DFG) (Contract CH 943/2-1). The authors would like to thank Wolfgang Dittus, and Stefan Paetel from Zentrum für Sonnenenergie- und Wasserstoff-Forschung Baden-Württemberg for preparing the CIGS absorber layer for this work.

References

1. Stanbery, B.J. Copper indium selenides and related materials for photovoltaic devices. *Crit. Rev. Solid State*. **27**, 73-117 (2002).
2. Kemell, M., Ritala, M., & Leskelä, M. Thin film deposition methods for CuInSe₂ solar cells. *Crit. Rev. Solid State*. **30**, 1-31 (2005).
3. Kazmerski, L.L. Solar photovoltaics R&D at the tipping point: a 2005 technology overview. *J. Electron Spectrosc.* **150** (2-3), 105-135 (2006).
4. Empa [Internet]. Empa.ch: A new world record for solar cell efficiency; [cited 2013 January 18]. Available from: <http://www.empa.ch/plugin/template/empa/3/131438/---/l=2> (2013).
5. Sadewasser, S., Glatzel, T., Schuler, S., Nishiwaki, S., Kaigawa, R., & Lux-Steiner, M.C. Kelvin probe force microscopy for the nano scale characterization of chalcopyrite solar cell materials and devices. *Thin Solid Films*. **431-432**, 257-261 (2003).
6. Jiang, C.S., Noufi, R., AbuShama, J.A., Ramanathan, K., Moutinho, H.R., Pankow, J., & Al-Jassim, M.M. Local built-in potential on grain boundary of Cu(In,Ga)Se₂ thin-films. *Appl. Phys. Lett.* **84**, 3477-1 - 3477-3 (2004).
7. Abou-Ras, D., Koch, C.T., Küstner, V., van Aken, P.A., Jahn, U., Contreras, M.A., Caballero, R., Kaufmann, C.A., Scheer, R., Unold, T., & Schock, H.W. Grain-boundary types in chalcopyrite-type thin films and their correlations with film texture and electrical properties. *Thin Solid Films*. **517**, 2545-2549 (2009).
8. Nichterwitz, M., Abou-Ras, D., Sakurai, K., Bundesmann, J., Unold, T., Scheer, R., & Schock, H.W., Influence of grain boundaries on current collection in Cu(In,Ga)Se₂ thin-film solar cells. *Thin Solid Films*. **517**, 2554-2557 (2009).
9. Abou-Ras, D., Schorr, S., & Schock, H.W. Grain sizes and grain boundaries in chalcopyrite-type thin films. *J. Appl. Cryst.* **40**, 841-848 (2007).
10. Niles, D.W., Al-Jassim, M., & Ramanathan, K. Direct observation of Na and O impurities at grain surfaces of CuInSe₂ thin films. *J. Vac. Sci. Technol. A* **17**, 291-296 (1998).
11. Rockett, A., Granath, K., Asher, S., Al Jassim, M.M., Hasoon, F., Matson, R., Basol, B., Kapur, V., Britt, J.S., Gillespie, T., & Marshall, C. Na incorporation in Mo and CuInSe₂ from production processes. *Sol. Energy Mater. Sol. Cells*. **59**, 255-264 (1999).
12. Heske, C., Eich, D., Fink, R., Umbach, E., Kakar, S., van Buuren, T., Bostedt, C., Terminello, L.J., Grush, M.M., Callcott, T.A., Himpfel, F. J., Ederer, D.L., Perera, R.C.C., Riedel, W., & Karg, F. Localization of Na impurities at the buried CdS/Cu(In, Ga)Se₂ heterojunction. *Appl. Phys. Lett.* **75**, 2082-2084 (1999).
13. Braunger, D., Hariskos, D. Bilger, G., Rau, U., & Schock, H.W. Influence of Na on the growth of polycrystalline Cu(In,Ga)Se₂ thin films. *Thin Solid Films*. **361**, 161-166 (2000).
14. Cerezo, A., Godfrey, T.J., Sijbrandij, S.J., Smith, G.D.W., & Warren, P.J. Performance of an energy-compensated three-dimensional atom probe. *Rev. Sci. Instrum.* **69**, 49-58 (1998).

15. Blavette, D., Bostel, A., Sarrau, J.M., Deconihout, B., & Menand, A. An atom-probe for three dimensional tomography. *Nature*. **363**, 432-435 (1993).
16. Gault, B., Vurpillot, F., Vella, A., Gilbert, M., Menand, A., Blavette, D., & Deconihout, B. Design of a femtosecond laser assisted tomographic atom probe. *Rev. Sci. Instrum.* **77**, 043705-1 - 043705-8 (2006).
17. Kelly, T.F. & Miller, M.K. Atom probe tomography. *Rev. Sci. Instrum.* **78**, 031101-1 - 031101-20 (2007).
18. Thompson, K., Lawrence, D., Larson, D.J., Olson, J.D., Kelly, T.F., & Gorman, B. *In situ* site-specific specimen preparation for atom probe tomography. *Ultramicroscopy*. **107** (2-3), 131-139 (2007).
19. Cadet, E., Barreau, N., Kessler, J., & Pareige, P. Atom probe study of sodium distribution in polycrystalline Cu(In,Ga)Se₂ thin film. *Acta Material*. **58**, 2634-2637 (2010).
20. Schlesiger, R., Oberdorfer, C., Würz, R., Greiwe, G., Stender, P., Artmeier, M., Pelka, P., Spaleck, F., & Schmitz, G. Design of a laser-assisted tomographic atom probe at Münster University. *Rev. Sci. Instr.* **81**, 043703 (2010).
21. Cojocaru-Mirédin, O., Choi, P., Abou-Ras, D., Schmidt, S.S., Caballero, R., & Raabe, D. Characterization of grain boundaries in Cu(In,Ga)Se₂ films using atom-probe tomography. *IEEE J. Photovolt.* **1** (2), 207-212 (2011).
22. Cojocaru-Mirédin, O., Choi, P., Wuerz, R., & Raabe, D. Atomic-scale characterization of the CdS/CuInSe₂ interface in thin-film solar cells. *Appl. Phys. Lett.* **98**, 103504-1 - 103504-3 (2011).
23. Couzinie-Devy, F., Cadet, E., Barreau, N., Arzel, L., & Pareige, P. Atom probe study of Cu-poor to Cu-rich transition during Cu(In,Ga)Se₂ growth. *Appl. Phys. Lett.* **99**, 232108-1 - 232108-3 (2011).
24. Voorwinden, G., Jackson, P., Kniese, R., & Powalla, M. In-line Cu(In,Ga)Se₂ co-evaporation process on 30 cm x 30 cm substrates with multiple deposition stages, Proceedings of the 22nd European Photovoltaic Solar Energy Conference. Milan, Italy, 2115-2118 (2007).
25. Miller, M.K., Russell, K.F., Thompson, K., Alvis, R., & Larson, D.J., Review of atom probe FIB-based specimen preparation methods. *Microscopy Microanal.* **13** (6), 428-436 (2007).
26. Vurpillot, F., Cerezo, A., Blavette, D., & Larson, D.J., Modeling image distortions in 3DAP. *Microscopy and Microanalysis*. **10** (3), 384-390 2 (2008).
27. Kellog, G.L. Determining the field emitter temperature during laser irradiation in the pulsed laser atom probe. *J. Appl. Phys.* **52**, 5320 (1981).
28. IVASTM 3.6.2 User Guide 2012, CAMECA Instruments, Inc. (2012).
29. Persson, C. & Zunger, A., Compositionally induced valence-band offset at the grain boundary of polycrystalline chalcopyrites creates a hole barrier. *Appl. Phys. Lett.* **87**, 211904-1 - 211904-3 (2005).
30. Zhang, S.B., Wei, S.-H., Zunger, A., & Katayama-Yoshida, H. Defect physics of the CuInSe₂ chalcopyrite semiconductor. *Phys. Rev. B*. **57**, 9642-9656 (1998).
31. Cahn, J.W. In: W.C. Johnson, J.M. Blakely (Eds.), *Interfacial Segregation*, American Society of Metals, Metals Park, OH, 3-23 (1979).
32. Miller, M.K. & Jayaram, R. Some factors affecting analysis in atom probe. *Surf. Sci.* **266**, 458-462 (1992).
33. Wuerz, R., Eicke, A., Kessler, F., Paetel, S., Efimenko, S., & Schlegel, C. CIGS thin-film solar cells and modules on enamelled steel substrates. *Sol. Energy Mat. Sol. Cells*. **100**, 132-137 (2012).
34. De Geuser, F., Lefebvre, W., Danoix, F., Vurpillot, F., Forbord, B., & Blavette, D. An improved reconstruction procedure for the correction of local magnification effects in three-dimensional atom-probe, *Surf. Interf. Anal.* **39**, 268-272 (2007).
35. Kingham, D.R. The post-ionization of field evaporated ions: A theoretical explanation of multiple charge states. *Surf. Sci.* **116**, 273-301 (1982).
36. Letellier, L. Etude des joints de grains et interphases dans les superalliages Astroloy par microscopie électronique et tomographie atomique, Ph.D. dissertation, Rouen Univ., Groupe Physique des Matériaux, Rouen, France, (1994).
37. Portavoce, A., Blum, I., Hoummada, K., Mangelinck, D., Chow, Lee, & Bernardini, J., Original methods for diffusion measurements in polycrystalline thin-films. *Defect and Diffusion Forum*. **322**, 129-150 (2012).